J Mater Sci (2019) 54:4732–4741

Computation

Theoretical insight into the optoelectronic properties of lead-free perovskite derivatives of $Cs_3Sb_2X_9$ (X = Cl, Br, I)

Yu-Liang Liu[1], Chuan-Lu Yang[1,*], Mei-Shan Wang[1], Xiao-Guang Ma[1], and You-Gen Yi[2]

[1] School of Physics and Optoelectronics Engineering, Ludong University, Yantai 26425, People's Republic of China
[2] Hunan Key Laboratory for High-Microstructure and Ultrafast Process, College of Physics and Electronics, Central South University, Changsha 410083, People's Republic of China

Received: 24 September 2018
Accepted: 18 November 2018
Published online: 27 November 2018

ABSTRACT

The lead-free perovskites derivatives of $Cs_3Sb_2X_9$ (X = Cl, Br, I) have been synthesized, but their photocatalytic properties are not explored. To evaluate the feasibility for the visible light catalytic performance, we calculate the structural, electronic, optical and charge transfer properties of $Cs_3Sb_2X_9$, based on the hybrid density functional theory of HSE06 with the projector augmented wave potential. The results show the decrease of band energy gaps and the redshift of absorption edges from X = Cl to I. The absolute potential of the valence band maximum and conduction band minimum is determined to justify the feasibility of the photocatalytic water splitting or CO_2 reduction. The calculated carrier mobilities reveal that the high electron mobilities of $Cs_3Sb_2I_9$ are beneficial to the reducing powers for hydrogen generation and CO_2 reduction. The present results indicate that $Cs_3Sb_2I_9$ is appropriate for the photocatalytic water splitting to produce hydrogen or the CO_2 reduction driven by the visible light.

Introduction

As one of the most abundant energy sources, solar energy is inexhaustible. Photocatalytic water splitting to generate hydrogen and photocatalytic reduction of CO_2 into fuels driven by sunlight are a kind of artificial photosynthesis processes that only require sunlight, water and a photocatalyst for realizing the conversion of solar energy into chemical energy. It is a sustainable strategy to apply solar energy and to address current energy crisis as well as to alleviate the environmental issues caused by CO_2 emissions, such as "the greenhouse effect." Therefore, it is indispensable to explore and develop the efficient photocatalysts with excellent optoelectronic properties such as high solar-light absorption and superior carrier mobilities to enhance the solar energy photochemical conversion efficiency.

Over the last few years, hybrid organic–inorganic lead halide perovskites have been extensively employed in optoelectronic applications, including

Address correspondence to E-mail: ycl@ldu.edu.cn

https://doi.org/10.1007/s10853-018-3162-y

photodetectors [1, 2], light-emitting diodes [3, 4], which can be ascribed to their excellent optoelectronic properties. Recently, some studies about the lead halide perovskites for photocatalytic applications such as the degradation of organic dyes, CO_2 reduction and hydrogen production have been reported [5–10]. However, the instability of lead-based perovskite and the toxicity of heavy metal lead restrict the maximization of commercial applications of lead halide perovskites. The first-principle calculations for $CsPbX_3$ (X = Cl, Br, I) [11–14] confirm that the prominent optoelectronic properties of the Pb-based perovskites are associated with the outermost ns^2 electronic configuration of Pb^{2+}. The hybridization of *s* orbitals with *p* orbitals between lead and halogen is responsible for the antibonding character at the valence band maximum (VBM) as shown in Fig. 1. Zakutayev et al. [15] have reported that the presence of antibonding orbitals usually makes the defect levels induced by any kind of intrinsic defects lie within valence band as resonances and does not bring about a deep trap state in the forbidden band. Like Pb^{2+}, the outermost electronic configuration of Sb^{3+} is also ns^2, which is a stable valence electronic configuration. Thus, perovskites based on Sb^{3+} are expected to be promising materials which not only possess the excellent optoelectronic properties like those of lead halide perovskites but are less toxic than Pb [16]. Recently, some investigations about antimony halide complexes [17–19] including Sb halide

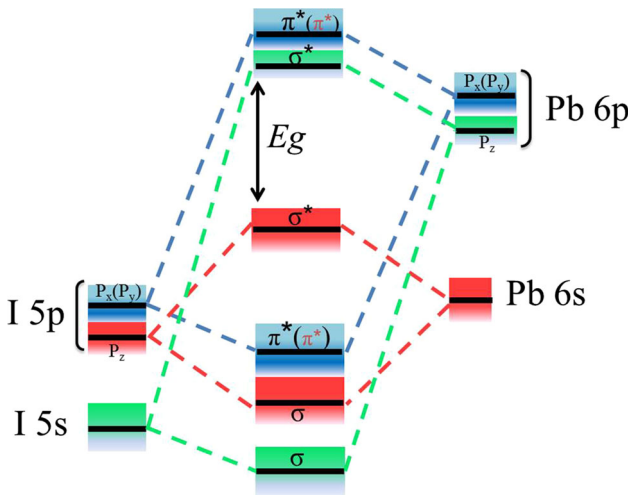

Figure 1 Schematic diagram of bonding (π_{pp}, σ_{pp}) and antibonding (π_{pp}*, σ_{pp}*) orbitals of $CsPbI_3$ showing the formation of the valence and conduction band. The π^{nb}_{pp} represents the non-bonding orbital.

complexes applicable to photodevices have been reported [20–22]. As a member of the Sb-based perovskites family, the cesium antimony halide perovskites with the formula of $Cs_3Sb_2X_9$ (X = Cl, Br, I) have attracted much interest due to their good stability. In 2000, Zemnukhova et al. [23] have reported that the $Cs_3Sb_2X_9$ (X = Cl, Br, I) perovskites can be prepared from CsX and SbX_3 aqueous solutions. Subsequently, more detailed studies for $Cs_3Sb_2X_9$ (X = Cl, Br, I) appeared in recent years. Remarkably, Saparov et al. [24] have reported that the layered structure of $Cs_3Sb_2I_9$ perovskite can be prepared by a two-step deposition approach and the density functional theory (DFT) calculations show that the optical absorption of $Cs_3Sb_2I_9$ is comparable to that of $CH_3NH_3PbI_3$. Moreover, the single crystal and quantum dots (QDs) for $Cs_3Sb_2Br_9$ have been synthesized by Song et al. [25]. Recently, Kuang et al. [26] have reported that their synthesized novel lead-free all-inorganic $Cs_2AgBiBr_6$ double perovskite nanocrystal shows an excellent performance for CO_2 reduction, implying the possibility of lead-free halide perovskites for photocatalytic applications. With these findings in mind, we explore the photocatalytic performance of $Cs_3Sb_2X_9$.

In the present work, we systematically investigate the photocatalytic properties of $Cs_3Sb_2X_9$ via calculating their electronic and optical properties by the first-principles hybrid DFT. The carrier mobility is calculated to examine the migration and separation of photogenerated electrons and holes. Our results indicate that $Cs_3Sb_2X_9$ has obvious absorptions in a wide range from near ultraviolet to visible light. Especially, $Cs_3Sb_2I_9$ exhibits a large absorption coefficient in the high-energy region of the visible light. The band edges alignments have been calculated to demonstrate that the positions of the band edges for $Cs_3Sb_2X_9$ straddle the corresponding absolute potentials of water splitting or CO_2 reduction. The present findings are expected to provide insights into the photocatalytic properties of $Cs_3Sb_2X_9$ and a helpful reference to develop the efficient photocatalytic materials.

Computational details

The cesium antimony halide perovskites derivatives with a formula of $A_3B_2X_9$ are derived from the traditional ABX_3-type perovskites with two-thirds of

occupancies of B site. As shown in Fig. 2a, b, Song et al. [25] have reported that the crystal structure of $Cs_3Sb_2Br_3$ ($P\ \bar{3}m1$, no. 164) can be constructed by removing every third Sb layer along <111> in $CsSbBr_3$ perovskites to achieve correct charge balance. The crystal lattices of $Cs_3Sb_2X_9$ are demonstrated in Fig. 2c. All the structures have been fully optimized by using a conjugate gradient algorithm with the exchange and correlation potentials of Perdew–Burke–Ernzerhof (PBE) [27] parameterization under the generalized gradient approximation (GGA). The convergence criteria of the total energy of the system and the forces on each atom are set to 10^{-6} eV and 0.01 eV/Å, respectively. The 5 × 5 × 5 Monkhorst–Pack *k*-point meshes are used for sampling the Brillouin zone, and the kinetic energy cutoff is set to 500 eV after a careful convergent test (Table 1). Since the PBE functional usually underestimates the band energy gap and the improvement effect of the Heyd–Scuseria–Ernzerhof (HSE06) hybrid functional [28] has been confirmed by Le Bahers and Sautet et al. [29–31], we employ the HSE06 hybrid functional to calculate the band energy structures and optical absorptions of $Cs_3Sb_2X_9$. All the calculations are carried out with the Vienna ab initio simulation package (VASP 5.4.4) [32, 33]. The core-valence interactions are described by the projected augmented wave (PAW) pseudopotentials method [34]. The choice of valence electrons for Cl, Br, I, Sb, Cs and Pb atoms is Cl ($3s^23p^5$), Br ($4s^24p^5$), I ($5s^25p^5$), Sb ($5s^25p^3$), Cs ($5s^25p^66s^1$) and Pb ($6s^26p^2$), respectively.

Table 1 Calculated lattice parameter *a*, *b*, *c* (Å), bond length of X-Sb (X = Cl, Br, I) (Å), band energy E_g (eV) of, $Cs_3Sb_2X_9$ (Cl, Br, I)

Species	Lattice constants			$B_{X\text{-}Sb}$	E_g
	a	*b*	*c*		
$Cs_3Sb_2Cl_9$					
Present	7.827	7.827	9.472	2.83	3.11
Exp.[1]	7.633[1]	7.633	9.345	–	3.09[2]
Error	2.5%	2.5%	1.3%	–	–
$Cs_3Sb_2Br_9$					
Present	8.138	8.138	9.943	2.97	2.60
Exp.	7.930[3]	7.930	9.716	–	2.30[3]
Error	2.6%	2.6%	2.3%	–	–
$Cs_3Sb_2I_9$					
Present	8.664	8.664	10.633	3.18	2.04
Exp.	8.420[4]	8.420	10.386	3.16[1]	2.05[4]
Error	2.8%	2.8%	2.4%	–	–
Theory	8.661[4]	8.661	10.625	–	2.06[4]

[1]Ref. [35]

[2]Ref. [38]

[3]Ref. [25]

[4]Ref. [24]

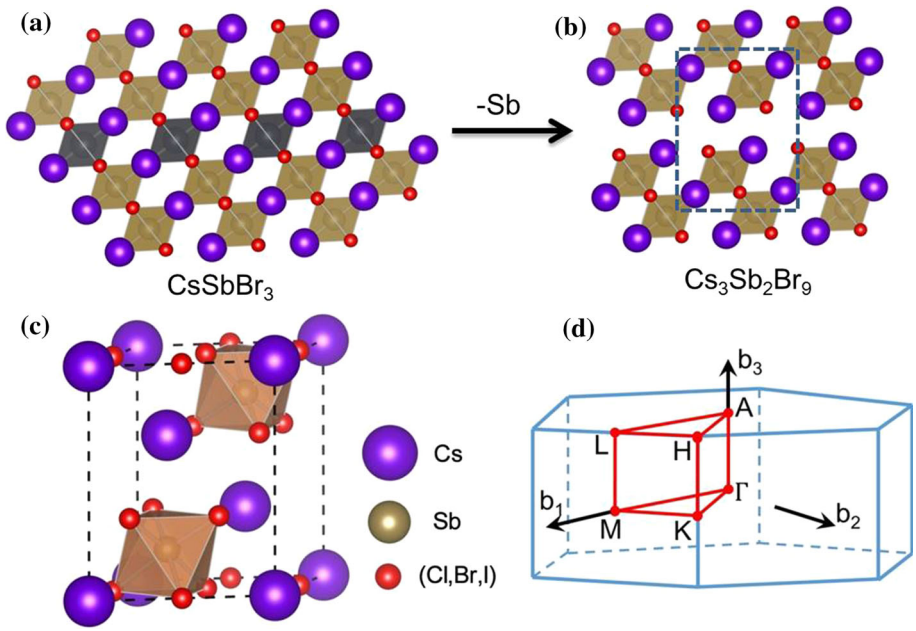

Figure 2 Removal of every third Sb layer along the <111> direction of **a** the perovskite structure results in **b** the 2D layered modification of $Cs_3Sb_2Br_9$. The purple, gray and red spheres represent Cs, Sb or Br elements, respectively. **c** The optimized structure of $Cs_3Sb_2Br_9$. **d** The selected high-symmetry lines in the Brillouin zone are Γ–M–K–Γ–A–L–H–A.

Results and discussion

Geometrical and band energy structures

The calculated lattice parameters, bond lengths of $Cs_3Sb_2X_9$, including the available experimental and the previous theoretical values, are presented in Table 1. From the table, we can see that the errors between the present lattice parameters of $Cs_3Sb_2X_9$ with their experimental values [24, 25, 35] are less than 3% and the results for $Cs_3Sb_2I_9$ are also consistent with the previous theoretical values [24], indicating that the present theoretical level is credible. The lattice parameters and the length of Sb–X bonds increase from $Cs_3Sb_2Cl_9$ to $Cs_3Sb_2I_9$, which can be understood from the fact that the effective radius of the X atom increases from Cl to I.

The calculated energy band structures of $Cs_3Sb_2X_9$ with PBE and HSE06 functional along with the high-symmetry k points in the Brillouin zone are shown in Fig. 3. One can observe from the figure that $Cs_3Sb_2Br_9$ and $Cs_3Sb_2I_9$ exhibit a direct band energy gap with the VBM and the conduction band minimum (CBM) located at Γ point. However, $Cs_3Sb_2Cl_9$ has an indirect band energy gap, because the VBM is located at Γ point but the CBM at A point (Fig. 3c). Although the PBE functional may underestimate the band energy gap of the semiconductor compared with the HSE06 hybrid functional, the contours of the energy levels remain a similar characteristic for the two calculational methods [36, 37]. The calculated band energy gaps for $Cs_3Sb_2X_9$ by HSE06 functional are listed in Table 1. The present 3.11, 2.60 and 2.04 eV for the band energy gaps of $Cs_3Sb_2X_9$ are in good agreement with the available experimental data [24, 25, 38] and the other theoretical values in the literature [24]. The total density of states (TDOS) and the partial density of states (PDOS) of $Cs_3Sb_2X_9$ can be used to understand the orbital characteristics of VBM and CBM. For $Cs_3Sb_2Cl_9$, as shown in Fig. 4a, the first interaction is the strong p–p interactions resulting from the overlap of Cl(3p)–Sb(5p) throughout most of the conduction band and the low energy part of the valence band, which leads to the antibonding characteristic of the CBM and the bonding one at the low energy zone of the valence band. The other one is the typical s–p interaction from the hybridization of Sb(5s) atomic orbitals and Cl(3p) atomic orbitals at the valence band, which is responsible for the presence of antibonding orbitals at VBM. Moreover, similar interactions can be found for $Cs_3Sb_2Br_9$ and $Cs_3Sb_2I_9$ but not are described here for the sake of brevity.

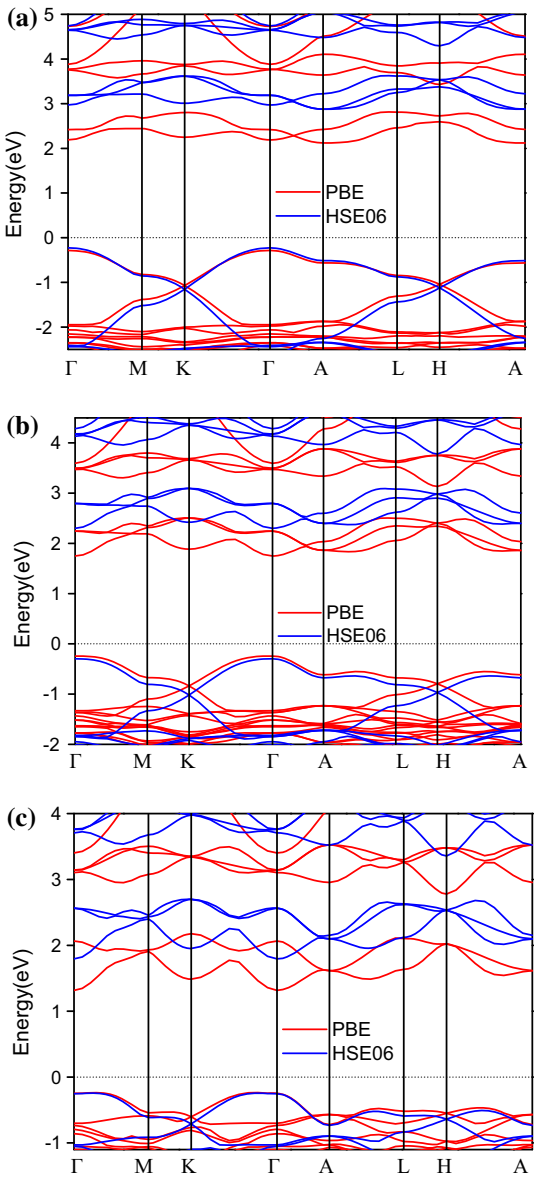

Figure 3 Band structures of **a** $Cs_3Sb_2Cl_9$, **b** $Cs_3Sb_2Br_9$, **c** $Cs_3Sb_2I_9$ calculated by PBE and HSE06 functional. The red solid lines and blue solid lines represent the PBE and the HSE06 results, respectively. The energy zero represents the Fermi level.

Absolute energy-level positions and feasibility for photocatalytic water splitting and CO_2 reduction

In a photocatalytic process, the semiconductor absorbs the light, transfers the electron at valence

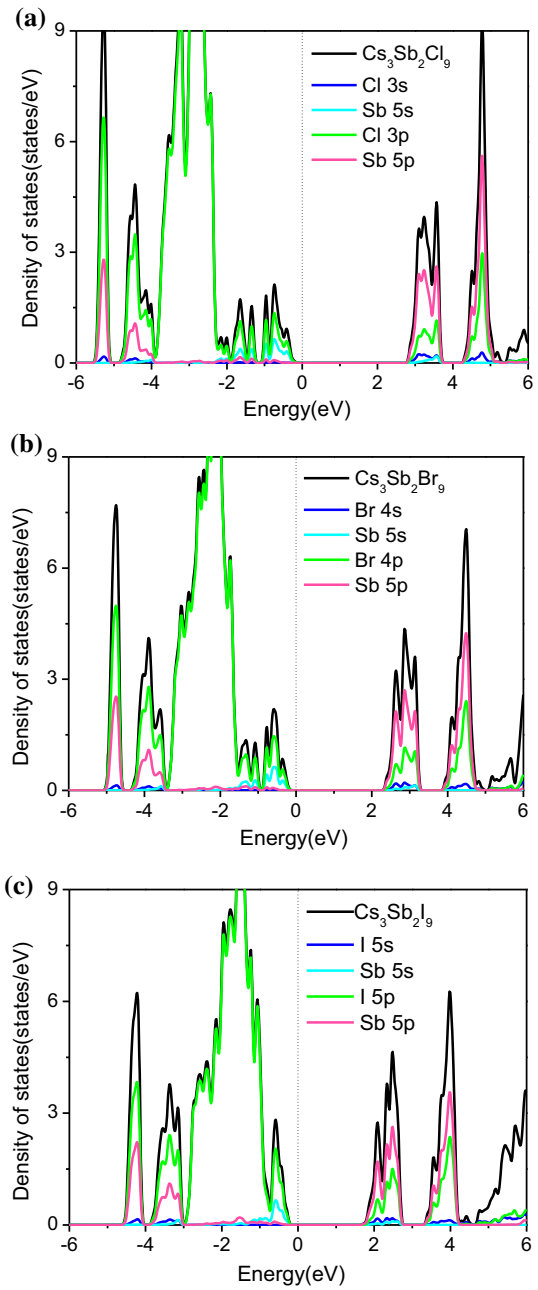

Figure 4 Total and partial density of states are calculated by HSE06 functional. **a** $Cs_3Sb_2Cl_9$; **b** $Cs_3Sb_2Br_9$; **c** $Cs_3Sb_2I_9$.

band to the conduction band and produces the photogenerated electron–hole pairs. Then, the photogenerated electrons and holes transfer to the corresponding reaction sites for the oxidation or reduction reactions. Accordingly, the absolute energy-level positions of CBM and VBM must satisfy the requirement of the photocatalytic reactions which can be described by two half reactions. Specifically, for the hydrogen evolution or CO_2 photoreduction to CH_4, the potential is determined according to the following half-reactions, respectively:

$$2H^+ + 2e^- \rightarrow H_2 \quad (1)$$

$$CO_2 + 8e^- + 8H^+ \rightarrow CH_4 + 2H_2O \quad (2)$$

while the half-reaction steps for the water oxidation of both reactions can be summarized as follows:

$$2H_2O + 4h^+ \rightarrow O_2 + 4H^+ \quad (3)$$

Therefore, the CBM for the water-splitting reaction should be higher than the reduction potential of H^+/H_2 ($E_{H^+/H_2} = -4.44$ eV at pH = 0.0). Similarly, CBM for the photoreduction of CO_2 should be more negative than the potentials for CO_2/CH_4 ($E_{CO_2/CH_4} = -4.62$ eV at pH = 0.0). On the other hand, the VBM should be lower than the oxidation potential of O_2/H_2O ($E_{O_2/H_2O} = -5.67$ eV at pH = 0.0). Obviously, it is crucial to calculate precisely the edge position of materials to evaluate the feasibility of photocatalytic water splitting and CO_2 reduction; especially, the surface chemistry and interfacial effects are considered in the process. Galli et al. [39] have summarized recent progress and open theoretical challenges present in simulations of PEC interfaces. They provide a good policy to treat the effect of the interface on the band position of the surface structure, in which the aqueous solution model has been considered. However, it is still a challenging task to establish a theoretical approach for predicting the absolute energy positions of CBM and VBM for the bulk structure. Here, we calculate the absolute band edges of $Cs_3Sb_2X_9$ based on a reliable approximate method supposed by Xu et al. [40] for a bulk semiconductor by the following equations:

$$E_{VBM} = \chi - \frac{1}{2}E_g \quad (4)$$

$$E_{CBM} = E_{VBM} + E_g \quad (5)$$

where E_{VBM} and E_{CBM} represent the absolute potentials of VBM and CBM. The χ is the electronegativity of the semiconductor which can be determined by the absolute electronegativities of the constituent atoms as:

$$\chi(\text{compound}) = \chi_1^a \chi_2^b \ldots \chi_n^c \quad (6)$$

where χ_1,χ_2 and χ_n represent the electronegativities of the atoms in the compound, while a, b and c are the molar fractions of the atoms. Here, the

electronegativity of atoms are evaluated by the Mulliken electronegativity as follows [41]:

$$\chi = (I + A)/2 \tag{7}$$

where I is the ionization energy and A is the electron affinity of the atom. The electronegativities of Cs, Sb, Cl, Br and I can be obtained using Eq. (7). Finally, the calculated values of E_{VBM} and E_{CBM} for $Cs_3Sb_2X_9$ at pH = 0 based on Formulas (4) and (5) are given in Table 2. The results show that the values of E_{VBM} for $Cs_3Sb_2Cl_9$, $Cs_3Sb_2Br_9$ and $Cs_3Sb_2I_9$ are − 7.15 eV, − 6.58 eV and − 5.92 eV, which are 1.48 eV, 0.91 eV and 0.25 eV lower than the water oxidation potential, respectively, while E_{CBM}s are about 0.40 eV, 0.46 eV and 0.56 eV higher than the hydrogen reduction potential, respectively. Therefore, $Cs_3Sb_2X_9$ satisfies the requirement of the absolute potentials of VBM and CBM for water-splitting reaction. Figure 5 visually expresses the absolute energy positions of band edges and the redox potentials of the water-splitting reaction and CO_2 reduction. The figure demonstrates that the absolute potential of CBM for $Cs_3Sb_2I_9$ is the most negative one among the three structures, which suggests that it is more efficient for hydrogen reduction. Moreover, all the positions of CBM for $Cs_3Sb_2X_9$ are higher than the reduction potential for CO_2 to CH_4 and their VBMs are located at a more positive position than the water oxidation potential, implying that the E_{VBM} and E_{CBM} satisfy the requirement of the CO_2 reduction reaction.

Optical absorption properties

The optical absorption coefficient $\alpha(\omega)$ can be used to evaluate the response ability of photocatalyst. A large absorption coefficient means more photons can be captured to impact on the photocatalytic performance. The $\alpha(\omega)$ can be obtained from the real parts $\varepsilon_1(\omega)$ and imaginary parts $\varepsilon_2(\omega)$ of the dielectric function via the following equation [42]:

Table 2 Calculated E_{VBM} (eV) and E_{CBM} (eV) for $Cs_3Sb_2X_9$(Cl, Br, I)

Species	E_{VBM}	E_{CBM}
$Cs_3Sb_2Cl_3$	− 4.04	− 7.15
$Cs_3Sb_2Br_3$	− 3.98	− 6.58
$Cs_3Sb_2I_3$	− 3.88	− 5.92

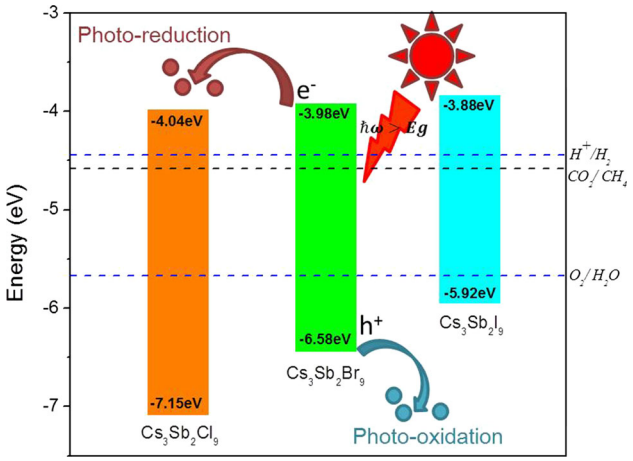

Figure 5 VBM and CBM positions of $Cs_3Sb_2X_9$(Cl, Br, I) with respect to water and CO_2 redox potential.

$$\alpha(\omega) = \sqrt{2}\omega\sqrt{\sqrt{\varepsilon_1^2(\omega) + \varepsilon_2^2(\omega)} - \varepsilon_1(\omega)} \tag{8}$$

Therefore, we first calculated the dielectric function of $Cs_3Sb_2X_9$ by employing HSE06 functional. The details of the calculation of the dielectric function can be found from the previous literature [43] and omitted here for brevity. The calculated $\varepsilon_2(\omega)$ of the dielectric function for $Cs_3Sb_2X_9$ is shown in Fig. 6a. The characteristics of $\varepsilon_1(\omega)$ and $\varepsilon_2(\omega)$ can be understood from the electronic properties. The contours of $\varepsilon_2(\omega)$ are well consistent with those of the total DOS in Fig. 4a. For example, the peak of $\varepsilon_2(\omega)$ for $Cs_3Sb_2I_9$ appears at around 2.8 eV corresponding to the electronic transition from VBM to the sharper peak of DOS at around 2.8 eV.

The calculated optical absorption coefficients for the three structures are presented in Fig. 6b. The optical absorption edge of $Cs_3Sb_2Cl_9$ occurred near the UV light region corresponding to its band energy gaps (E_gs) of 3.1 eV, while that of the other two structures shows a continuous redshift. For $Cs_3Sb_2Br_9$, a large absorption coefficient of about 40000 cm^{-1} has been identified in the high-energy region of the visible light. Notably, $Cs_3Sb_2I_9$ exhibits a more obvious and wider absorption around the peak at about 3.0 eV in the visible light range, which mainly comes from the transition from I 5p states to Sb 5p states. The larger absorption coefficient suggests that more photons could be captured in the corresponding light range, which is a benefit to generate electron–hole pairs. In the sense, $Cs_3Sb_2I_9$ is

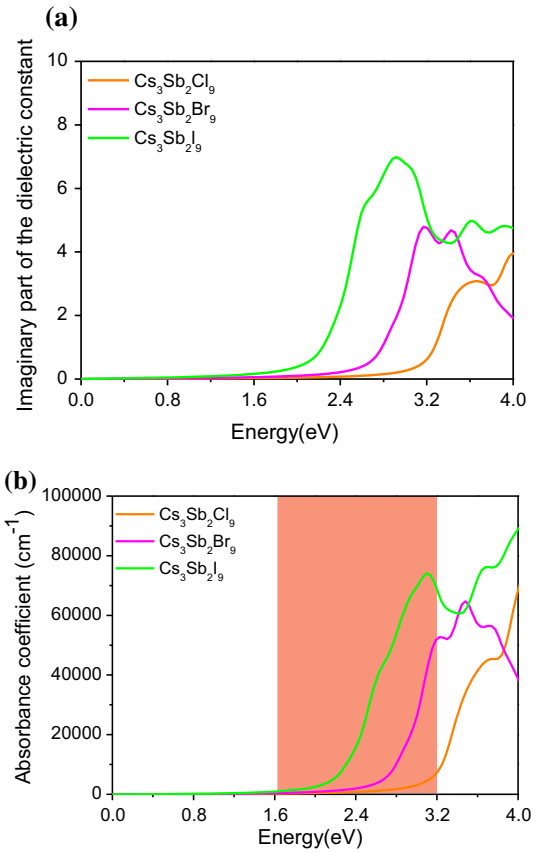

Figure 6 **a** Imaginary part of the dielectric function and **b** absorption coefficient of $Cs_3Sb_2X_9$(Cl, Br, I).

the most efficient one of the three structures to respond to the visible light in the photocatalysis.

Migration and separation of photogenerated electron–hole pairs

The charge spatial separation and the migration rate of the photogenerated charge pair play a key role in the practical photocatalysis. The carrier mobility can give a quantitative description of the transferring ability of the photoinduced charges. The higher carrier mobility implies that charge transfer is more efficient. Moreover, the larger mobility differences between the electrons and the holes are more significant for separation of the photogenerated electron–hole pairs.

The carrier mobility can be calculated via the deformation potential (DP) theory by the following formula [44–46]:

$$\mu = \frac{2\sqrt{2\pi}e\hbar^4 B}{3m_I^*(m_b^* k_B T)^{\frac{3}{2}}E^2} \quad (9)$$

where e, $\hbar$, k_B and T represent the electron charge, reduced Planck constant, Boltzmann constant and temperature, respectively. B is the bulk modulus defined as $B = V_0\left(\partial^2 E_{\mathrm{tot}}/\partial V^2\right)$, where E_{tot} is the total energies of the systems and V_0 is the equilibrium volume of the system. E is the deformation potential constant determined by $E = \left(\Delta E_{\mathrm{edge}}\right)/(\Delta V/V_0)$, where ΔV is the variation of volume caused by changing lattice parameters and E_{edge} is the corresponding change of the energy for CBM or VBM. The conductivity effective mass $m_I^* = 3(1/m_x^* + 1/m_y^* + 1/m_z^*)^{-1}$ and the DOS effective mass $m_b^* = (m_x^* m_y^* m_z^*)^{1/3}$ are evaluated by calculating the effective mass along the x, y and z directions, respectively.

By employing the similar treats of Lv et al. [36] and Chin et al. [46], we estimated the effective masses of electrons (m_e*) and holes (m_h*) in different directions by PBE functional with the equation: $m^* = \pm\hbar^2\left(\frac{d^2E_k}{dk^2}\right)^{-1}$. The calculated m_x*, m_y*, m_z*, m_I* and m_b* of electrons and holes for all structures are summarized in Table 3. Considering the high carrier mobility is the obvious characteristic of the lead halide perovskites, we also calculated the carrier mobility of $CsPbBr_3$ as a contrast for that of $Cs_3Sb_2X_9$. The spin–orbit coupling (SOC) effects have been employed to overcome the degeneracy of energy level of $CsPbBr_3$ in the electronic properties calcula-

Table 3 Calculated effective masses (m*s) of electrons and holes in the unit of free electron mass and other works for pristine $CsPbBr_3$, $Cs_3Sb_2X_9$(Cl, Br, I)

Species	Electrons			Holes		
	m_x*	m_y*	m_z*	m_x*	m_y*	m_z*
$CsPbBr_3$	0.25	0.25	0.22	0.25	0.27	0.23
$CsPbBr_3^{other}$	0.15[1]	0.14	0.15	0.16[1]	0.15	0.15
$Cs_3Sb_2Cl_3$	0.71	0.71	0.66	1.00	1.00	0.64
$Cs_3Sb_2Br_3$	0.29	0.29	0.53	2.98	2.98	0.44
$Cs_3Sb_2I_3$	0.21	0.21	0.39	1.05	1.05	0.44

[1]Ref. [47]

Table 4 Calculated conductivity effective mass $m_l^*(m_0)$, density-of-states effective mass $m_b^*(m_0)$ and elastic constant B (eV/Å^3), deformation potential constant E (eV), carrier mobility μ (cm^2 V^{-1} s^{-1}) of the

	$Cs_3Sb_2Cl_9$		$Cs_3Sb_2Br_9$		$Cs_3Sb_2I_9$		$CsPbBr_3$	
	Electrons	Holes	Electrons	Holes	Electrons	Holes	Electrons	Holes
m_l^*	0.69	0.84	0.34	1.02	0.25	0.72	0.24	0.25
m_b^*	0.69	0.86	0.35	1.58	0.26	0.79	0.24	0.25
B	0.16	0.16	0.13	0.13	0.11	0.11	0.13	0.13
E	9.97	11.55	9.06	10.26	9.01	9.89	7.73	10.42
μ	3.9	1.7	22.1	1.1	56.8	1.9	75.4	38.5

tion due to the heavy element lead (Fig. S1). The calculated results of $CsPbBr_3$ are in agreement with those of Yettapu et al. [47]. Table 3 demonstrates that m_x^*, m_y^* of electron or hole for $Cs_3Sb_2X_9$ are equivalent but different from their m_z^*, which can be ascribed to the same arrangement in x and y directions. It implies that the transport properties of $Cs_3Sb_2X_9$ are anisotropic for both electron and hole. The bulk modulus B and the deformation potential constant E were calculated by fitting parabolic functions of the total energy and band edge positions toward unit strain, respectively. The results are shown in Fig. S2. Finally, the calculated values of m_l^*, m_b^*, B, E, μ are summarized in Table 4.

As we can see from the table that the calculated mobility of electron and hole for $CsPbBr_3$ is 75.4 cm^2 V^{-1} s^{-1} and 38.5 cm^2 V^{-1} s^{-1}, which is consistent with the experimental 52.0 cm^2 V^{-1} s^{-1} and 11.0 cm^2 V^{-1} s^{-1} of Bakr et al. [48], respectively. It is worth mentioning that the electron mobility of $Cs_3Sb_2I_9$ reaches 75% of that of $CsPbBr_3$, although that of $Cs_3Sb_2Cl_9$ and $Cs_3Sb_2Br_9$ is obviously small. The high electron mobility of $Cs_3Sb_2I_9$ implies that the photogenerated electrons can rapidly transfer from the inside to the surface of the semiconductor for the proton reduction reaction. In addition, the differences between mobilities of the electron and the hole for $Cs_3Sb_2I_9$ are more obvious in comparison with those of $CsPbBr_3$, which will significantly reduce the recombination rate of the photogenerated carriers and enhance the photocatalytic activity of $Cs_3Sb_2I_9$. In this sense, $Cs_3Sb_2I_9$ is more suitable for efficient photocatalysis than the other $Cs_3Sb_2X_9$.

Conclusions

In conclusion, we have investigated the feasibility of $Cs_3Sb_2X_9$ in the photocatalytic water splitting to produce hydrogen or CO_2 reduction by using the first-principles DFT with the HSE06 hybrid functional. The results reveal that all the three structures have appropriate band edges for the water splitting and CO_2 reduction reactions. It is worth noting that one most suitable band energy gap of 2.04 eV is identified for $Cs_3Sb_2I_9$, which corresponds to an obvious absorption in the visible light range. Unlike the other two structures, the mobility of the electrons for $Cs_3Sb_2I_9$ is close to that of the lead perovskite $CsPbBr_3$, which implies that the rapid migration of photogenerated charge pairs is also possible for $Cs_3Sb_2I_9$. Moreover, the large differences between the mobilities of the electron and hole for $Cs_3Sb_2I_9$ could decrease the recombination rate of electron and hole and enhance the photocatalytic performance. To sum up, $Cs_3Sb_2I_9$ is a promising candidate for the photocatalytic CO_2 reduction or water splitting to produce hydrogen driven by the visible light on the basis of the optimal band energy gap with the appropriate band edges, the strong visible light absorption and the large electron mobility.

Acknowledgements

This work was supported by the National Natural Science Foundation of China (NSFC) under Grant Nos. NSFC-11874192 and NSFC-11574125, as well as the Taishan Scholars Project of Shandong Province (ts201511055).

Electronic supplementary material: The online version of this article (https://doi.org/10.1007/s10853-018-3162-y) contains supplementary material, which is available to authorized users.

References

[1] Dou L, Yang YM, You J, Hong Z, Chang WH, Li G (2013) Solution-processed hybrid perovskite photodetectors with high detectivity. Nat Commun 5:5404

[2] Fang Y, Huang J (2015) Resolving weak light of sub-picowatt per square centimeter by hybrid perovskite photodetectors enabled by noise reduction. Adv Mater 27:2804–2810

[3] Li G, Tan ZK, Di D, Lai ML, Jiang L, Lim JH (2015) efficient light-emitting diodes based on nano-crystalline perovskite in a dielectric polymer matrix. Nano Lett 15:2640–2644

[4] Kim YH, Cho H, Heo JH, Kim TS, Myoung NS, Lee CL (2015) multicolored organic/inorganic hybrid perovskite light-emitting diodes. Adv Mater 27:1248–1254

[5] Gao G, Xi Q, Zhou H, Zhao Y, Wu C, Wang L (2017) Novel inorganic perovskite quantum dots for photocatalysis. Nanoscale 33:12032–12038

[6] Lim SC, Lin HP, Tsai WL, Lin HW, Hsu YT, Tuan HY (2017) Binary halide, ternary perovskite-like, and perovskite-derivative nanostructures: hot injection synthesis and optical and photocatalytic properties. Nanoscale 9:3747–3751

[7] Schünemann S, Van GM, Tüysüz H (2018) A $CsPbBr_3/TiO_2$ composite for visible-light driven photocatalytic benzyl alcohol oxidation. Chemsuschem 13:2057–2061

[8] Xu YF, Yang MZ, Chen BX, Wang XD, Chen HY, Kuang DB (2017) A $CsPbBr_3$ perovskite quantum dot/graphene oxide composite for photocatalytic CO_2 reduction. J Am Chem Soc 139:5660

[9] Park S, Chang WJ, Chan WL, Park S, Ahn HY, Nam KT (2016) Photocatalytic hydrogen generation from hydriodic acid using methylammonium lead iodide in dynamic equilibrium with aqueous solution. Nat Energy 2:16185

[10] Wang X, Wang H, Zhang H, Yu W, Wang X, Zhao Y (2018) Dynamic interaction between methylammonium lead iodide and TiO_2 nanocrystals leads to enhanced photocatalytic H_2 evolution from HI splitting. Acs Energy Lett 5:1159–1164

[11] Filippetti A, Mattoni A (2014) Hybrid perovskites for photovoltaics: insights from first principles. Phys Rev B 89:231–236

[12] Kang J, Wang LW (2017) High defect tolerance in lead halide perovskite $CsPbBr_3$. J Phys Chem Lett 8:489–493

[13] Kim J, Lee SH, Lee JH, Hong KH (2014) The role of intrinsic defects in methylammonium lead iodide perovskite. J Phys Chem Lett 5:1312–1317

[14] Yin WJ, Shi T, Yan Y (2014) Unusual defect physics in $CH_3NH_3PbI_3$ perovskite solar cell absorber. Appl Phys Lett 104:063903

[15] Zakutayev A, Caskey CM, Fioretti AN, Ginley DS, Vidal J, Stevanovic V (2014) Defect tolerant semiconductors for solar energy conversion. J Phys Chem Lett 5:1117–1125

[16] Hebig JC, Kühn I, Flohre J, Kirchartz T (2016) Optoelectronic properties of $(CH_3NH_3)_3Sb_2I_9$ thin films for photovoltaic applications. Acs Energy Lett 1:309–314

[17] Yang B, Li YJ, Tang YX, Mao X, Luo C, Wang MS (2018) Constructing sensitive and fast lead-free single-crystalline perovskite photodetectors. J Phys Chem Lett 9:3087–3092

[18] Harikesh PC, Mulmudi HK, Ghosh B, Goh TW, Teng YT, Thirumal K (2016) Rb as an alternative cation for templating inorganic lead-free perovskites for solution processed photovoltaics. Chem Mater 28:7496–7504

[19] Zuo C, Ding L (2017) Lead-free perovskite materials $(NH_4)_3Sb_2I_xBr_{9-x}$. Angew Chem 129:6628–6632

[20] Adonin SA, Frolova LA, Sokolov MN, Shilov GV, Korchagin DV, Fedin VP, Aldoshin SM, Stevenson KJ, Troshin PA (2018) Antimony (V) complex halides: lead-free perovskite-like materials for hybrid solar cells. Adv Energy Mater 8:1701140

[21] Adonin SA, Bondarenko MA, Abramov PA, Novikov AS, Plyusnin PE, Sokolov MN, Fedin VP (2018) Bromo- and polybromoantimonates(V): structural and theoretical studies of hybrid halogen-rich halometalate frameworks. Chem Eur J 24:10165–10170

[22] Adonin SA, Udalova LI, Abramov PA, Novikov AS, Yushina IV, Korolkov IV, Semitut EY, Derzhavskaya TA, Stevenson KJ, Troshin PA, Sokolov MN, Fedin VP (2018) A novel family of polyiodo-bromoantimonate(III) complexes: cation-driven self-assembly of photoconductive metal-polyhalide frameworks. Chem Eur J 24:14707–14711

[23] Zemnukhova LA, Kuznetsov SI, Fedorishcheva GA, Davidovich RL (2000) The temperature dependence of $^{121,123}Sb$, ^{35}Cl, $^{79,81}Br$ and ^{127}I NQR spectra in complexes $Cs_3Sb_2X_9$ (X = Cl, Br, I). Z Naturforsch 55:134–138

[24] Saparov B, Hong F, Sun JP, Duan HS, Meng W, Cameron S (2015) Thin-film preparation and characterization of $Cs_3Sb_2I_9$: a lead-free layered perovskite semiconductor. Chem Mater 27:5622–5632

[25] Zhang J, Yang Y, Deng H, Farooq U, Yang X, Khan J (2017) High quantum yield blue emission from lead-free inorganic antimony halide perovskite colloidal quantum dots. ACS Nano 11:9294–9302

[26] Zhou L, Xu YF, Chen BX, Kuang DB, Su CY (2018) Synthesis and photocatalytic application of stable lead-free $Cs_2AgBiBr_6$ perovskite nanocrystals. Small 14:1703762

[27] Perdew JP, Burke K, Ernzerhof M (1996) Generalized gradient approximation made simple. Phys Rev Lett 77:3865–3868

[28] Le Bahers T, Rérat M, Sautet P (2014) Semiconductors used in photovoltaic and photocatalytic devices: assessing fundamental properties from DFT. J Phys Chem C 118:5997–6008

[29] Melissen ST, Labat F, Sautet P, Le Bahers T (2015) Electronic properties of $PbX_3CH_3NH_3$ (X = Cl, Br, I) compounds for photovoltaic and photocatalytic applications. Phys Chem Chem Phys 17:2199–2209

[30] Lardhi S, Curutchet A, Cavallo L, Harb M, Le Bahers T (2017) Ab initio assessment of $Bi_{1-x}RE_xCuOS$ (RE = La, Gd, Y, Lu) solid solutions as a semiconductor for photochemical water splitting. Phys Chem Chem Phys 19:12321–12330

[31] Heyd J (2003) Hybrid functionals based on a screened Coulomb potential. J Chem Phys 118:8207–8215

[32] Kresse G, Furthmüller J (1996) Efficiency of ab initio total energy calculations for metals and semiconductors using a plane-wave basis set. Comput Mater Sci 6:15–50

[33] Kresse G, Furthmüller J (1996) Efficient iterative schemes for ab initio total-energy calculations using a plane-wave basis set. Phys Rev B Condens Matter 54:11169–11186

[34] Blöchl PE (1994) Projector augmented-wave method. Phys Rev B Condens Matter 50:17953–17979

[35] Yamada K, Sera H, Sawada S, Tada H, Okuda T, Tanaka H (1997) Reconstructive phase transformation and kinetics of $Cs_3Sb_2I_9$ by means of rietveld analysis of X-Ray diffraction and ^{127}I NQR. J Solid State Chem 134:319–325

[36] Lv X, Wei W, Sun Q, Li F, Huang B, Dai Y (2017) Two-dimensional germanium monochalcogenides for photocatalytic water splitting with high carrier mobility. Appl Catal B 217:275–284

[37] Liu X, Sohlberg K (2015) The influence of oxygen vacancies and La doping on the surface structure of $NaTaO_3$. Comput Mater Sci 103:1–7

[38] Timmermans CWM, Cholakh SO, Blasse G (1983) The luminescence of $Cs_3Bi_2Cl_9$ and $Cs_3Sb_2Cl_9$. J Solid State Chem 46:222–233

[39] Pham TA, Ping Y, Galli G (2017) Modelling heterogeneous interfaces for solar water splitting. Nat Mater 16:401–408

[40] Xu Y, Schoonen MAA (2000) The absolute energy positions of conduction and valence bands of selected semiconducting minerals. Am Mineral 85:543–556

[41] Mulliken RS (1934) A new electroaffinity scale; together with data on valence states and on valence ionization potentials and electron affinities. J Chem Phys 2:782

[42] Lin Y, Jiang Z, Zhu C, Hu X, Zhu H, Zhang X (2013) The optical absorption and hydrogen production by water splitting of (Si, Fe)-codoped anatase TiO_2 photocatalyst. Int J Hydrogen Energy 38:5209–5214

[43] Liu YL, Yang CL, Wang MS, Ma XG, Yi YG (2018) Te-doped perovskite $NaTaO_3$ as a promising photocatalytic material for hydrogen production from water splitting driven by visible light. Mater Res Bull 107:125–131

[44] He Y, Galli G (2014) Perovskites for solar thermoelectric applications: a first principle study of $CH_3NH_3AI_3$ (A = Pb and Sn). Chem Mater 26:5394–5400

[45] Wang H, Pei Y, Lalonde AD, Snyder GJ (2012) Weak electron-phonon coupling contributing to high thermoelectric performance in n-type PbSe. P Natl Acad Sci USA 109:9705–9709

[46] Chin XY, Cortecchia D, Yin J, Bruno A, Soci C (2015) Lead iodide perovskite light-emitting field-effect transistor. Nat Commun 6:7383

[47] Yettapu GR, Talukdar D, Sarkar S, Swarnkar A, Nag A, Ghosh P (2016) THz conductivity within colloidal $CsPbBr_3$ perovskite nanocrystals: remarkably high carrier mobilities and large diffusion lengths. Nano Lett 16:4838–4848

[48] Saidaminov MI, Haque MA, Almutlaq J, Sarmah S, Miao XH, Begum R (2017) Inorganic lead halide perovskite single crystals: phase-selective low-temperature growth, carrier transport properties, and self-powered photodetection. Adv Opt Mater 5:1600704